# Excitation transfer in barium by collisions with noble gases

J. Brust and A.C. Gallagher
*Joint Institute for Laboratory Astrophysics, National Institute of Standards and Technology and University of Colorado, Boulder, Colorado 80309-0440*

(Received 5 December 1994; revised manuscript received 4 May 1995)

We present a time-resolved study of excitation transfer processes between the low-lying excited states of barium ($6s6p\,^3P_J$, $6s5d\,^1D_2$, $6s5d\,^3D_J$) induced by collisions with noble gases. The transient excited-state populations have been measured by means of fluorescence and absorption spectroscopy. Cross sections for spin-changing collisions from $^3P_1$ to $^1D_2$ and from $^1D_2$ to $^3D_3$ as well as for fine-structure mixing within the $^3D$ multiplet were obtained by fitting the numerical solution of a seven-state system of rate equations including diffusion to the experimental data. We compare our results to experimental findings for other alkaline earth metals and report an improved value of the lifetime of the $6s6p\,^3P_1$ state of barium.

PACS number(s): 34.30.+h, 34.50.−s, 32.70.Cs

## I. INTRODUCTION

Electronic excitation transfer processes in metal vapors induced by thermal collisions with noble-gases have been the subject of many experimental and theoretical investigations over the past three decades. Due to its simplicity the fine-structure transfer within the resonance doublets of the alkali metals [1–3] served as a model case for atomic collision processes. These measurements and calculations, together with investigations of spectral line broadening, redistribution of resonance radiation, and other collisonal phenomena, have improved our understanding of interatomic interactions and the nonadiabatic mechanisms underlying inelastic atomic collisions. These are important to our understanding of various kinds of astrophysical and technical plasmas. Recently it has been shown that theory can reliably predict the cross section for fine-structure transfer in alkaline earth ions in a temperature range relevant for astrophysical applications [4,5]. In recent years interest has shifted to more complex atoms such as the alkaline earth and group IIB metal atoms, in which spin changes as well as fine-structure changing collisions can be studied. This tests our understanding gained in the study of the alkali and alkali-like atoms and ions.

Experimental and theoretical studies have been done primarily for the alkaline earth metals. For Mg there exist *ab initio* potential curves and close-coupling calculations of the fine-structure transfer within the lowest $^3P$ states [6], but to our knowledge there have been no measurements of this process.

Calcium has been studied extensively. Wright and Balling [7] as well as Harris *et al.* [8] investigated the collision induced cascade between the $4\,^1P_1$ and the $4\,^3P_J$ states of Ca, although the failure to monitor the populations of the intermediate $^1D_2$ and $^3D$ states led to a misinterpretation of the dominant transfer channel. Breckenridge and Merrow [9] measured the branching ratios of the $4\,^1P_1$ quenching, finding the surprising result that, in contradiction to Wigner's spin rule, this process is dominated by the $^1P \rightarrow {}^3D$ rather than the $^1P_1 \rightarrow {}^1D_2$ transfer as proposed by Harris *et al.* The latter seemed more likely since the $^1D_2$ state is located energetically between the $^1P_1$ and the $^3D_J$ states.

Hale *et al.* [10,11] measured the noble-gas-induced transfer between the $5\,^1P_1$ state and nearby levels as well as its dependence on the initial alignment of the collision complex. As in the case of the $4\,^1P_1$ state they found a propensity for singlet-triplet transfer, although this is not as surprising as in the case of the $4\,^1P_1$ state since $5\,^3P$ is energetically much closer to $5\,^1P_1$ than is $3\,^1D_2$.

Theoretical calculations of the relevant potential energy curves and the collision dynamics for Ca-He collisions have been reported [12–14]. The pseudopotential calculations and Landau-Zener-type dynamical analysis of Zagrebin and Tserkovnyi [14] show good agreement with Hale and Leone's $5\,^1P_1$ quenching data but overestimate the cross section for the $4\,^1P_1 \rightarrow 3\,^3D_J$ transfer by a factor of 4. Nonetheless, they were able to explain the absence of $^1P$-$^1D$ transfer by a strong configuration interaction between the $^1\Sigma(^1D_2)$ molecular orbital correlated to the $3\,^1D_2$ state with the molecular orbitals of the same symmetry originating from the $4\,^1P_1$ and higher lying $^1\Sigma$ states.

Yuh and Dagdigian [15] experimentally investigated the fine-structure transfer within the $4\,^3P$ states of Ca induced by He collisions. Close-coupling calculations of the collision dynamics of this system by Alexander *et al.* [16] using potential curves published by Malvern [17] yielded only poor agreement with the experimental values.

The same propensity for collisional transfer between singlet and triplet states as in Ca has been found in Sr–noble-gas collisions [7,18,19]. In contrast to the fine-structure mixing in calcium, which was found to have a gas kinetic cross section, the fine-structure transfer within the $5s5p\,^3P_J$ of Sr turned out to be very small, as would be expected for nearly adiabatic collisions [20]. For the heavy noble-gases Kr and Xe, the authors found that fine-structure transfer is caused by three-body rather than two-body collisions.

 

Collisional deactivation of the resonance state ($6\,^1P_1$) in Ba by collisions with noble-gases has been studied by Breckenridge and Merrow [21]. They report an exclusive production of $6\,^3P_2$. This transfer to the closest $^3P_J$ state appears reasonable since the large spin-orbit splitting in the $6\,^3P_J$ should not favor a crossing with the lower $J$ states or fine-structure transfer in the outgoing half collision. The absence of the latter is consistent with the fine-structure transfer measurement of Kelly *et al.* in Sr [20]. Several rate coefficients for inter- and intramultiplet mixing involving $6\,^1P_1$, $6\,^3P_J$, $5\,^1D_2$, and $5\,^3D_J$ have been derived from experiments investigating the dynamics of resonantly pumped Ba vapors in He and Ar [22,23]. As in the case of Sr, no calculations of the cross sections are available.

The present work is aimed toward the completion of investigations of noble-gas induced multiplet mixing processes in the low-lying states of the heavier alkaline earth metals. Together with the promising progress in the theoretical treatments of alkaline earth metal–noble-gas atom systems this should lead to a better understanding of this processes.

Figure 1 shows the reduced level scheme of barium with the radiative and collisional transitions relevant for this work. To study the excitation transfer processes we used pulsed laser radiation to excite ground-state Ba atoms into the $6\,^3P_1$ state, which decays radiatively as well as collisionally into the lower-lying $5\,^{1,3}D$ states. Time-resolved measurement of the population densities of the $^3P$, $^1D_2$, and $^3D_J$ states was achieved by measuring the absorption of appropriate spectral lines from a Ba hollow cathode lamp, as well as the fluorescence from the $^3P_1$ state. Numerical fitting of the measured densities to the solution of a seven-state rate equation model identifies the major collision channels and provides the related transfer rates.

## II. EXPERIMENTAL DETAILS

### A. Measurements

Figure 2 shows the experimental apparatus. The cell containing the Ba vapor and the noble gas (NG) was a resistively heated stainless steel oven [24]. The temperature in our experiment ranged from 750 to 900 K, with corresponding Ba densities between $5 \times 10^{10}$ and $5 \times 10^{12}$ cm$^{-3}$. Absorption measurements of the excited-state populations were taken at the higher Ba densities to obtain line absorptions of 2–30 % under the various experimental conditions. The $6\,^3P_1$ lifetime studies were done at low Ba densities (770 K) to avoid radiation trapping. In order to absorb most of the laser light in the excitation-detection region (Fig. 3) two water-cooled copper tubes extended from the arms into the center of the cell, confining the Ba vapor to a length of about 2 cm in the direction of the laser beam (for a detailed description of the cell see [24]). The excited atoms were produced by the output of a frequency-stabilized external cavity GaAs diode laser tuned to the $6\,^1S_0$–$6\,^3P_1$ intercombination transition of Ba at 791.138 nm. The continuous laser output was modulated by an acousto-optic modulator producing square pulses of 500 ns–20 $\mu$s length with a period of 1 ms. The pulse rise and fall times were on the order of 150 ns. The peak laser power upon entering the cell was about 3 mW and a typical beam diameter was 2.6 mm. Typical absorption measurements employed 10- and 20-$\mu$s pulses to produce a sufficient density of excited atoms. For fluorescence measurements of the $^3P_1$ lifetime we used 1-$\mu$s pulses to reduce the buildup of population in the metastable states.

The transient excited-state populations were obtained from the absorption of emission lines from a hollow cathode lamp light passing through the cell perpendicular to

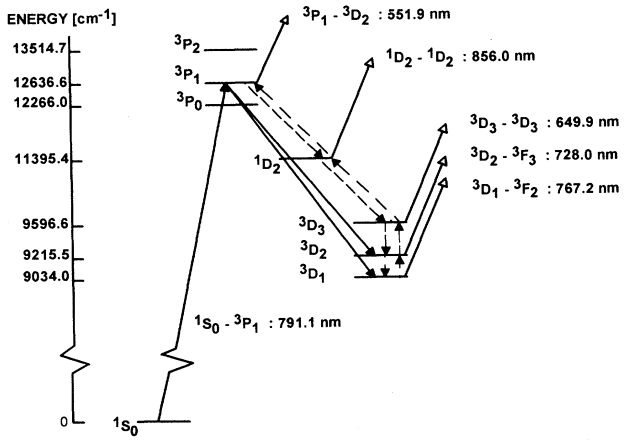


FIG. 1. Reduced level scheme of Ba showing the states under investigation. Solid arrows represent radiative transitions and dashed arrows the dominant collisional channels as found in the experiment.

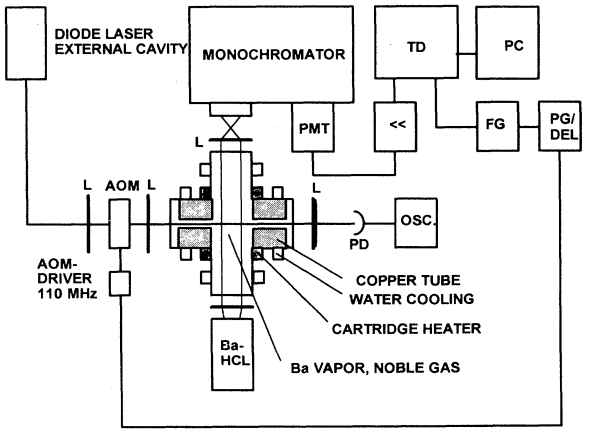


FIG. 2. Experimental setup: AOM, acousto-optic modulator; PD, photodiode; HCL, hollow cathode lamp; PMT, photomultiplier; TD, transient digitizer; FG, function generator; PG/DEL, pulse/delay generator; L, lenses; PC, personal computer.

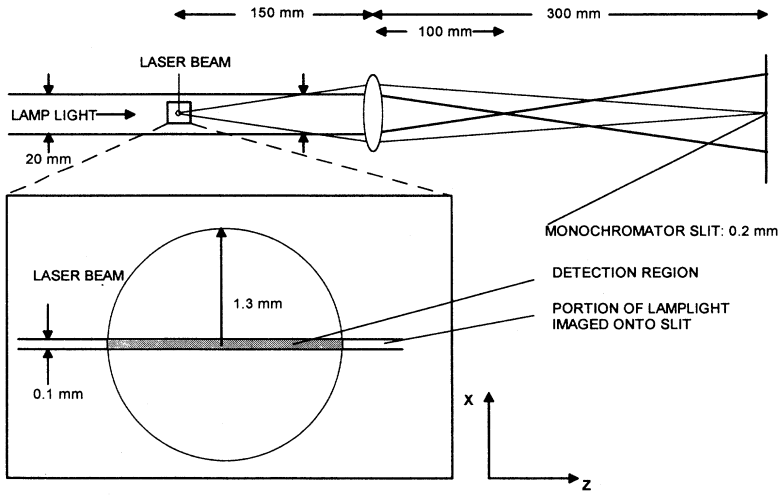


FIG. 3. Detection geometry of the absorbtion measurements. The collimated beam from the hollow cathode lamp (diameter approximately equal to 20 mm) crosses the laser beam (diameter approximately equal to 2.6 mm) at the center of the cell. The 2:1 imaging of the 200-$\mu$m monochromator slit into the cell results in the detection of a 100-$\mu$m cord of the excited-state population as shown in the inset.

the laser beam (Figs. 2 and 3). These lines were checked for self-inversion by measuring the absorption for different lamp currents, and for possible background contributions from lamp lines in the spectral vicinity.

The light of the hollow cathode lamp was passed through the cell as a parallel beam. The lens behind the cell imaged the laser beam onto the slit of a monochromator, which was tuned to select Ba emission lines terminating at the level under investigation (Fig. 1, Table II). The monochromator entrance slit (height equal to 5 mm) was oriented parallel to the laser beam and the width of entrance and exit slit were set to 200 $\mu$m. This optical arrangement probes a slice of about 100 $\mu$m height through a cord of the approximately cylindrical excited atom distribution (Fig. 3). As will be described below, this detection geometry was crucial to account for diffusion in our experiment. Since the exact length of the absorption path was not known and furthermore was changing with time, the quantity measured was a column population density

$$n(x,y,t) = \int_{-\infty}^{\infty} n(x,y,z,t)dz. \tag{1}$$

For the sake of brevity, however, we will refer to it as population density throughout the text.

The transient change in transmitted lamp light intensity as well as the $^3P_1$ fluorescence was detected through the monochromator by a photomultiplier tube whose amplified signal was measured and stored by a 50-MHz transient digitizer. The accuracy of the digitizer time base is specified to be better than 0.1% by the manufacturer and was experimentally confirmed to be better than 1%, using a function generator and an electronic counter. The linearity of the detection system was checked by a set of neutral density filters.

Each measurement consisted of an absorption signal with laser and lamp on, plus a background signal with the hollow cathode lamp blocked to account for ambient light and for energy pooling fluorescence resulting from collisions of excited barium atoms [24]. For Ar, Kr, and Xe pressures of 15 hPa and above the $^3D_J$ atoms diffused so slowly that it was neccessary to account for the metastable state population produced by the preceding laser pulses. To correct for this background contribution we measured an absorption transient during 80 $\mu$s preceding the laser pulse and extrapolated this result linearly into the region of the absorption transient. In a typical measurement we averaged over $8 \times 10^5$ pulses and achieved an absorption detection limit better than 0.5%.

### B. Modeling of the kinetics

The time behavior of the excited-state populations is described by a set of rate equations with a diffusion term included

$$\dot{\boldsymbol{n}}(\boldsymbol{r},t) = -\underline{\mathcal{D}}\nabla^2\boldsymbol{n}(\boldsymbol{r},t) + \underline{\mathcal{C}}\boldsymbol{n}(\boldsymbol{r},t). \tag{2}$$

Here $\boldsymbol{n}$ is a vector having the excited as well as the ground-state populations as components. $\underline{\mathcal{D}}$ denotes a diagonal matrix containing the diffusion coefficients $D_i$ of the levels involved, whereas $\underline{\mathcal{C}}$ describes the radiative and collisional coupling between the states. $\underline{\mathcal{C}}$ contains 42 collisional rates representing all possible collisional transfer processes between the seven excited states. This number can be cut in half by applying the principle of detailed balance to relate forward and reverse rates.

Due to the coupling of spatial and temporal degrees of freedom by the diffusion term and the ground-state depletion due to optical pumping into the $5\,^3D_J$ states, this system of equations does not lend itself to easy solution. The latter problem can be accounted for by using the measured $6\,^3P_1$ population vs time as the source term of a system of rate equations that includes the excited states only. In this formulation the partial emptying of the ground state is included in the measured $^3P_1$ population and one can neglect the ground state in the calculations provided there is no collisional excitation of Ba atoms. This possibility can be excluded since the excition energy of the lowest excited Ba states is large compared

to the kinetic energy of the collisions.

In order to use the $^3P_1$ population as a source term for our model the corresponding experimental signal had to have a good signal-to-noise (S/N) ratio. This could only be achieved by using the $^3P_1$ fluorescence signal because the population densities in the $^3P_1$ were too small to cause more than 3% absorption of the lamp light. Since the fluorescence detection was not calibrated we used only the experimental time behavior of the $^3P_1$ fluorescence and determined the corresponding absolute values of the population density from our fit. This calibration procedure provides better accuracy than if the absorption signal were directly measured, because the error of the oscillator strength available from the literature of the transition used to probe the $^3P_1$ is 30%.

The other major complication in the solution of Eq. (2) is the coupling of space and time degrees of freedom due to diffusion, which requires full treatment of the spatial evolution of the excited atom distribution. This, however, can be avoided if one assumes identical diffusion coefficients for all excited states. In this case one can decompose $\boldsymbol{n}(\boldsymbol{r},t)$ into a diffusion $\mathcal{D}(\boldsymbol{r},t)$ and a collisional contribution $\mathcal{N}(t)$, where $\boldsymbol{n}(\boldsymbol{r},t) = \mathcal{D}(\boldsymbol{r},t)\times\mathcal{N}(t)$. Since the binding energy and the electronic structure of the $^{1,3}D$ states is similar, this should be a good approximation for them. For the $^3P$ states this approximation is of minor importance since the lifetimes of these levels are short compared to the diffusion time. Complications might arise in the case of a long residence time in the $^1D_2$ state, a possibility that is discussed Sec. III B. For our experimental geometry the diffusion problem is one dimensional (Fig. 3), since loss due to diffusion only happens perpendicular to the plane of the laser and the lamp radiation. If during the time of the measurement the excited atoms do not reach the cell walls, the boundary conditions for the excited-state population densities in the diffusion problem can be chosen to be zero at infinity. In this case and approximating the laser beam profile by a Gaussian the solution to the diffusion equation is

$$\mathcal{D}(x,t) = \frac{1}{\sqrt{\pi[\sigma_b^2 + 4D(t-t_0)]}} \times \exp\left(-\frac{x^2}{\sigma_b^2 + 4D(t-t_0)}\right), \quad (3)$$

where $x$ is the coordinate perpendicular to the plane of the laser and the lamp light, $D$ the diffusion coefficient, and $\sigma_b$ the $1/e$ halfwidth of the laser beam. Furthermore, due to the probe geometry depicted in Fig. 3, where the height of the probed volume is small compared to the width of the laser beam, the only time dependence is given by that at $x$ =0:

$$\mathcal{D}(x=0,t) = \frac{1}{\sqrt{\pi[\sigma_b^2 + 4D(t-t_0)]}}. \quad (4)$$

To calculate the solution of Eq. (2) for a given set of collisional rates, a diffusion coefficient and a given $^3P_1$ fluorescence transient, we first solved numerically the collisional part of Eq. (2) with a unit source term at $t_0$ = 0. This solution was multiplied by the right-hand side of Eq. (4) to account for diffusion and then convolved with the $^3P_1$ fluorescence transient. From the resulting population densities and the experimental signals, a normalized $\chi^2$ was calculated and minimized. The fitting parameters were the collisional transfer rates, the diffusion coefficient, and the $^3P_1$ peak population density. Since the solutions of Eq. (2) depended on the fitting parameters they had to be calculated for every minimization step, making the data reduction very time consuming. The correctness of the model developed above was supported by good agreement (within 20%) with the diffusion constants reported by Walker *et al.* [25] (Table I).

TABLE I. Diffusion coefficients at STP. In addition to the statistical error given below, we estimate a systematical error of 15% from the determination of the beam diameter $\sigma_b$ in Eq. (4).

| Noble gas | $D$ This work ($cm^2\,s^{-1}$) | Ref. [25] |
|---|---|---|
| Ne | $0.215 \pm 0.012$ | $0.201 \pm 0.016$ |
| Ar | $0.141 \pm 0.029$ | $0.143 \pm 0.011$ |
| Kr | $0.088 \pm 0.011$ | |
| Xe | $0.073 \pm 0.008$ | $0.084 \pm 0.008$ |

### C. Transition probabilities

The dominant experimental uncertainty is introduced by the poor knowledge of transition probabilities in Ba [26–29]. This holds as well for the transitions used to probe the excited-state populations as for the infrared transitions of the multiplet $6\,^3P_J \rightarrow 5\,^3D_J$. The precision of the literature values ranges from ±10% to ±50%. To produce consistent fits of our data we had to adjust most of the transition probabilities within their stated accuracy. The corrected values have been determined by measuring absorption with the excited-state populations in equilibrium, as well as by requiring conservation of overall number density. The latter requirement affects in particular the transfer from $6\,^3P_J$ to $5\,^1D_2$, since using the values reported in the literature one finds a $^1D_2$ population rate that is about 30% larger than the $^3P_1$ depopulation rate. Tables II and III show the tran-

TABLE II. Wavelength and transition probabilities of the transitions used to probe the excited-state population.

| Transition | $\lambda_{air}$ (nm) | $A^a$ | $A_{lit}$ ($10^8\ s^{-1}$) |
|---|---|---|---|
| $6s6d\,^3D_3$-$6s6p\,^3P_2$ | 577.8 | | $0.65 \pm 0.13^b$ |
| $6s6d\,^3D_2$-$6s6p\,^3P_1$ | 551.9 | | $0.50 \pm 0.17^c$ |
| $6s6d\,^3D_1$-$6s6p\,^3P_0$ | 542.5 | | $0.77^d$ |
| $5d6p\,^3D_3$-$6s5d\,^3D_3$ | 649.9 | 0.39 | $0.49 \pm 0.24^c$ |
| $5d6p\,^3F_3$-$6s5d\,^3D_2$ | 728.0 | 0.28 | $0.28 \pm 0.05^d$ |
| $5d6p\,^3F_2$-$6s5d\,^3D_1$ | 767.2 | 0.15 | $0.15 \pm 0.02^d$ |
| $5d6p\,^1D_2$-$6s5d\,^1D_2$ | 856.0 | 0.29 | $0.23 \pm 0.03^d$ |

[a]This work.
[b]Reference [29].
[c]Reference [27].
[d]Reference [26].
[e]Reference [28].

TABLE III. Transition probabilities of the infrared transitions originating from $6\,^3P_1$.

| Transition | $\lambda_{air}$ (nm) | This work $A$ ($10^5$ s$^{-1}$) | Ref. [30] |
|---|---|---|---|
| $6s6p\,^3P_1$-$6s^2\,^1S_0$ | 791.14 | $2.99 \pm 0.38$ | $2.99 \pm 0.38$ |
| $6s6p\,^3P_1$-$6s5d\,^3D_1$ | 2775.1 | $1.23 \pm 0.12$ | $1.48 \pm 0.15$ |
| $6s6p\,^3P_1$-$6s5d\,^3D_2$ | 2922.4 | $3.18 \pm 0.32$ | $3.85 \pm 0.38$ |

sition wavelength and the radiative transition rates finally used to obtain self-consistency in the data reduction. The branching coefficients for the transitions from $6\,^3P_1 \rightarrow 5\,^3D_{1,2}$ were calculated assuming $LS$ coupling, using our improved value for the $^3P_1$ lifetime and the value reported by Parkinson and Tomkins [30] for the intercombination line oscillator strength. It should be noted that we thus determined ratios of the transition probabilities of the probe transitions and the absolute values given in Table II were obtained by assuming the value for the transition $5d6p\,^3F_3 - 6s5d\,^3D_2$ to be correct. If all transition probabilities are decreased by 15% their values will be within the error limits of the literature data.

### D. Measurements involving helium

In a set of preliminary measurements in pure He, we found that with minimum pressure neccessary to protect the windows from the Ba vapor the collisional processes were still too fast for the time resolution of our experiment. Furthermore, the fast diffusional loss resulted in a poor S/N ratio in our absorption measurements. Therefore we prepared 10:1 and 20:1 mixtures of Kr and He, using the Kr to confine the Ba vapor; Kr was chosen because it had been found to cause the smallest multiplet mixing. To produce the mixture we used two volumes of our vacuum system separated by a valve, one of which contained the oven. Using the capacitance manometer we determined the effective volume ratio with a hot oven. The mixture was then prepared by opening the valve after filling each volume with a known pressure of Kr and He, respectively. After preparing the mixture we measured the $^3P_1$ fluorescence lifetime and found that the gases were completely mixed after a few minutes. Nevertheless we allowed for another 60 min of mixing time before we started the measurements. From a comparison of calculated pressures and pressures found after the mixing procedure we estimate the He partial pressure used in the data reduction to be accurate within 10%.

## III. RESULTS

The complete system of 7 states is described by 21 unknown collisional rates, after applying detailed balance to the ratios of forward and backward rates. A $\chi^2$ fit to the data including all of these collisional rates was not feasible since the data are not sensitive to some rates and it thus was not possible to identify the absolute minimum of the $\chi^2$. Therefore, we adopted an iterative approach where we started with a small set of fitting parameters that was chosen to reproduce the major characteristics of the systems behavior. In a second step we allowed for more processes to contribute and it turned out that the actual number of channels contributing significantly to the excitation transfer between the Ba levels under investigation is much smaller than 21.

The most important characteristics of the system can be discussed using the data presented in Fig. 4, which show the measured and fitted population densities of the $^1D_2$, $^3D_3$, and $^3D_2$ states vs time for three different Ne densities. Here the $^3P_J$ and $^3D_1$ transients, which will be discussed below, have been omitted for clarity. The beginning and the end of the laser pulse, which can be considered a square pulse on the time scale of Fig. 4, are marked by arrows. On the time scale of this figure the population of the directly excited $^3P_1$ state follows the laser pulse and is also omitted for clarity. With increasing Ne density the peak population densities of $^1D_2$ and $^3D_3$ rise compared to the peak population density in $^3D_2$ state, which is populated radiatively from the $^3P_1$ state. A close inspection shows that the $^1D_2$ and $^3D_2$ populations rise linearly at the beginning of the laser pulse, while the $^3D_3$ population shows a quadratic time dependence. This indicates a direct collisional transfer from $^3P_1$ into $^1D_2$, whereas the $^3D_3$ state is populated by a

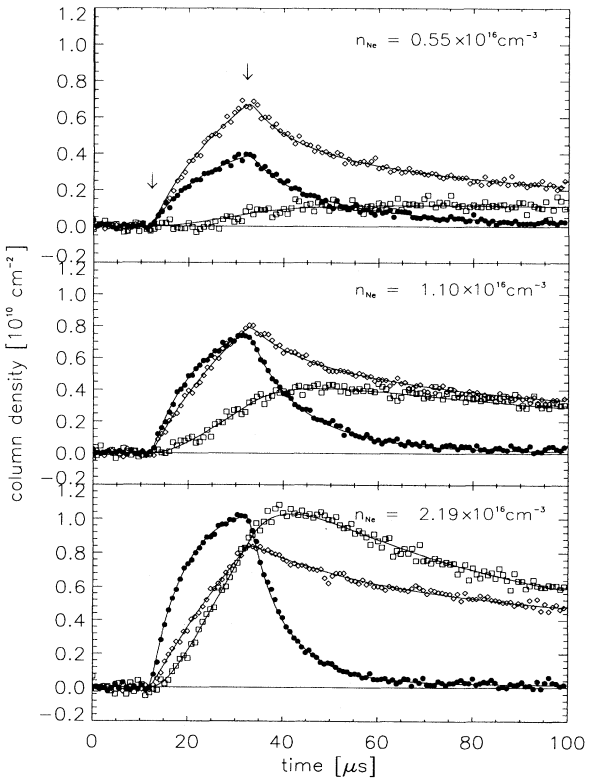


FIG. 4. Measured and fitted population densities of the $^1D_2$ (•), $^3D_3$, (□), and $^3D_2$ (◊) states for three Ne densities (0.55, 1.10, 2.2×10$^{16}$ cm$^{-3}$, $T$ =880 K, $\tau_p$ = 20 μs). Arrows indicate the beginning and end of the $6\,^3P_1$ excitation pulse.

two-step process. This could be explained by a cascade $^3P_1 \xrightarrow{k} {}^1D_2 \xrightarrow{k} {}^3D_3$ or $^3P_1 \xrightarrow{A} {}^3D_2 \xrightarrow{k} {}^3D_3$, where the latter includes a radiative transition from $^3P_1$ to $^3D_2$. $A$ and $k$ denote radiative and collisional transitions, respectively. Since the peak population of the $^3D_3$ state rises faster than linearly with pressure, we conclude that the $^3D_3$ state is populated by two collisional transfer processes rather than by a radiative and a collisional process. This conclusion is corroborated by the third set of transients in Fig. 4 taken at a Ne density of $2.2 \times 10^{16}$ cm$^{-3}$. The $^3D_3$ population density rises above the $^3D_2$ population density, whereas detailed balancing predicts a density ratio of 0.73:1. This shows that the $^3D_3$ state is predominantly populated from the $^1D_2$ state and that this process is the major transfer channel between the $^1D_2$ and the $^3D_J$ states. The $^3D_1$ population density is not shown in the plot to avoid overlap. At the beginning of the laser pulse the ratio $n(^3D_1)/n(^3D_2)$ matches the branching ratio of the radiative transitions originating from the $^3P_1$ state. As time progresses this changes toward the equilibrium population ratio, indicating that the $^3D_1$ state is populated radiatively from the $^3P_1$ state and collisionally predominantly from the $^3D_2$ state.

For the reasons discussed above, the data presented in Fig. 4, and equivalent data for the other gases, were initially fitted taking into account only four collisional channels. We assumed, in agreement with our qualitative discussion above, that an atom initially in the $^3P_1$ state is transferred only into the $^1D_2$ state and this collisionally transfers only into the $^3D_3$ state. The $^3D_J$ fine-structure mixing was assumed to occur only between neighboring levels. The fits shown in Fig. 4, and equivalent fits for the other gases, which were done using only these four transfer channels, yielded a very good description of the evolution of the excited-state population densities with time. Once the dominant rate coefficients were thus established, we relaxed our assumptions by adding more collisional channels, thereby establishing upper limits for the other rate coefficients. We now present the results for the different processes beginning with the results of the $^3P_1$ fluorescence measurements, which provide additional information about collisional processes involving the $^3P_1$ state.

### A. $6\,^3P_1$ fluorescence measurements

Figure 5 shows a time-dependent $6\,^3P_1$ fluorescence signals for Ar and Ne densities of $6.25\times10^{16}$ cm$^{-3}$ at a temperature of $T$ =775 K. The decay of both fluorescence signals shows double exponential behavior indicating collisional coupling of the $6\,^3P_1$ state to another state. While the decay rate of the first exponential decay is about the same for Ar and Ne, the second decay rate is significantly larger for Ne than for Ar. Double exponential behavior was observed with all noble-gases except He and is attributed to the return of excited-state population to the $6\,^3P_1$ state from a second state that is collisionally populated from the $6\,^3P_1$ state. The second exponential decay

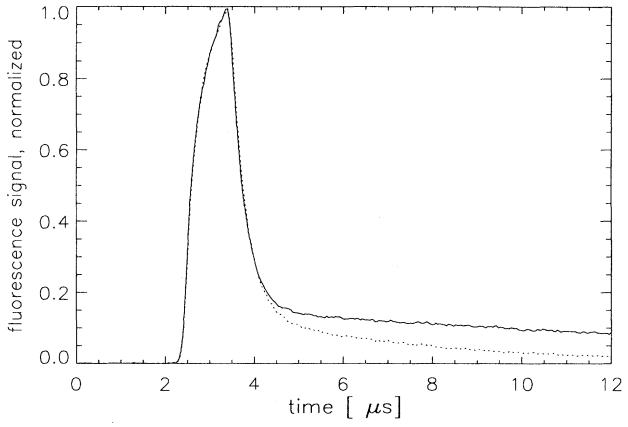


FIG. 5. $^3P_1$ fluorescence signal recorded at Ar (−) and Ne (···) densities of $6.25\times10^{16}$cm$^{-3}$, $T$ =775 K, $\tau_p = 1$ $\mu$s. The fluorescence decay shows double exponential behavior due to the collisional coupling between the $^3P_1$ and $^1D_2$ states.

was most prominent for noble-gas densities above $3\times10^{16}$ cm$^{-3}$. As discussed above, the absorption measurements demonstrated that the second state is the $5\,^1D_2$ state. This conclusion is confirmed by the fact that the $^3P_0$ and $^3P_2$ states, which also might cause double exponential behavior, have lifetimes of 2.4 $\mu$s and 1.3 $\mu$s [31], which are inconsistent with the decay rate of the second exponential decay (Fig. 5). The $^3D_J$ states can be ruled out since their energy separation from the $^3P_1$ state is much larger than $kT$ (Fig. 1) and because the absorption measurements discussed above showed that the collisional coupling between $^3P_1$ and $^3D_J$ proceeds through the $^1D_2$ state.

In order to analyze the observed fluorescence decay we used a simplified two-state rate equation model without diffusion, which included the radiative decay of the $6\,^3P_1$ state, the collisional transfer rates between the $6\,^3P_1$ and $5\,^1D_2$ states, and a collisional quenching rate for the $5\,^1D_2$ state. The neglect of diffusion in the model seemed justified due to the short radiative lifetimes of the $6\,^3P_1$ state and due to the fact that the second exponential decay of the the fluorescence signal, which was much slower than the first decay, was significant at higher pressures where diffusion has a minor effect. The two-state rate equation model can be solved analytically and yields the following expressions for the two decay constants $\lambda_\pm$:

$$\lambda_\pm = \frac{1}{2}(A_1 + R_{12} + R_2 + R_{21}) \pm \frac{1}{2}\sqrt{(A_1 + R_{12} - R_2 - R_{21})^2 + 4R_{12}R_{21}}. \quad (5)$$

The indices 1 and 2 denote the $6\,^3P_1$ and the $5\,^1D_2$ states, respectively. $A_1$ is the radiative decay rate of the $6\,^3P_1$ state and $R_2$ is a collisionally induced decay rate of the $5\,^1D_2$ state. $R_{12}$ and $R_{21}$, which are related by detailed balancing, represent the collisional transfer rate between the two states. The rates $R_{12}$ and $R_{21}$ were related using detailed balancing. To first order $\lambda_+$ represents the total

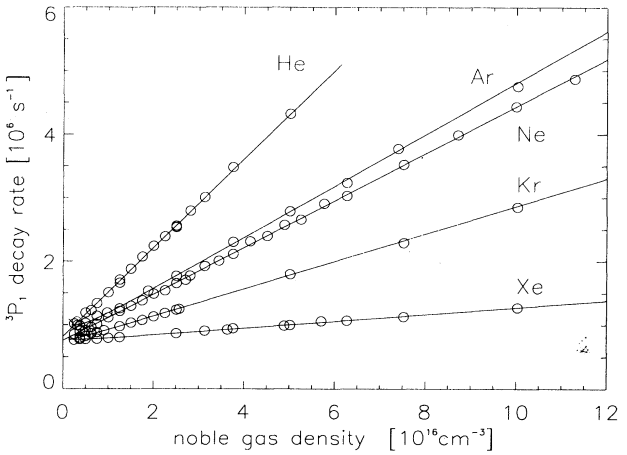


FIG. 6. $^3P_1$ fluorescence decay rate $\lambda_+$ vs noble-gas density, $T$=775 K. The solid lines were determined by a least-squares fit of a two-state rate equation model to the experimental decay rates.

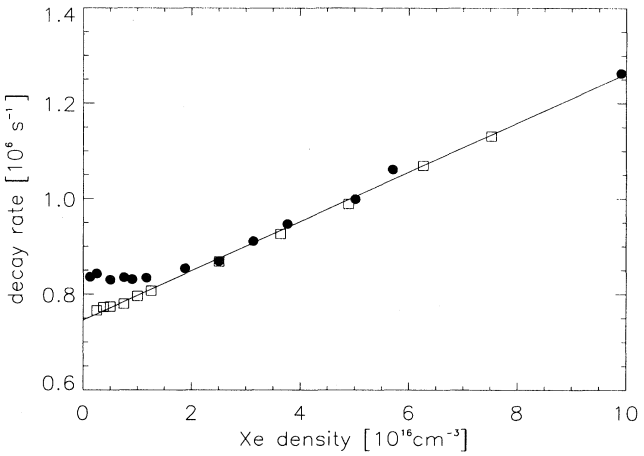


FIG. 7. $^3P_1$ decay rate $\lambda_+$ vs Xe pressure. Full circles (open squares) are data recorded with a slit width of 200 $\mu$m (2 mm) and 0.5 (3) magnification of the slit into the cell.

decay rate of the $^3P_1$ state, $A_1+R_{12}$, while $\lambda_-$ is the total decay rate of the $^1D_2$ state, $R_2+R_{21}$. Figure 6 shows the measured $\lambda_+$ vs noble-gas density for all noble-gases at a temperature of 775 K. The solid lines represent the fit of Eq. (5) to the two decay rates determined from the biexponential fit of the fluorescence signal. Table IV presents the rate coefficients for the $^3P_1$-$^1D_2$ transfer and for the depletion of the $^1D_2$ state derived from $6\,^3P_1$ fluorescence measurements at 775 K and 880 K.

At noble-gas densities below $1.5\times10^{16}$ cm$^{-3}$ the measured decay rates were affected by diffusion. This can be seen in Fig. 7, where the full circles represent the decay rate $\lambda_+$ vs Xe density measured with the imaging parameters described in the experimental section. At Xe densities below $1.5\times10^{16}$ cm$^{-3}$ the measured decay rate strongly deviates from the linear pressure dependence expected for $\lambda_+$ in Eq. (5). The deviation to higher decay rates at low pressures indicates a diffusion of the excited atoms out of the detection region, which was not accounted for by the simple rate equation model. For the fits of the two decay rates to the two-state model, only data taken at densities above $1.5\times10^{-16}$ cm$^3$ were used. For all noble-gases these fits yielded radiative decay rates of the $^3P_1$ state that were about 10% smaller than the literature value of $8.3\times10^5$ s$^{-1}$ [32]. To establish an accurate radiative lifetime, the measurement described in the next paragraph was made.

Due to the diffusion-induced deviations of the measured decay rates at low noble-gas densities, we never observed decay rates below the radiative rate of reference [32], when using the standard experimental geometry. We therefore decreased the diffusion contribution by opening the monochromator slit and changing the imaging optics to detect a region of about 6 mm height in the oven, as opposed to the 0.1 mm used for the previous measurements. The open squares in Fig. 7 show the resulting $^3P_1$ decay rate vs Xe density for the changed imaging parameters. This decay rate follows to low Xe densities the expected linear density dependence that was found at higher densities. The radiative decay rate of the $^3P_1$ state was established by extrapolating the measured rates to zero noble-gas density. Averaging this result and the results obtained from the previous fits for the different noble-gases we found a radiative decay rate of $(7.4\pm0.3)\times10^5$ s$^{-1}$, which is about 12% smaller than the value reported by Bucka and Nagel [32], which had a stated accuracy of $\pm10\%$.

### B. $6\,^3P_1$–$5\,^1D_2$ transfer

The fluorescence measurements provide a first source of information about the collisional processes involving the $^3P_1$ and $^1D_2$ states. The absorption measurements pro-

TABLE IV. Rate coefficients for $^3P_1$-$^1D_2$ transfer and quenching of the $^1D_2$ state in $10^{-12}$ cm$^3$ s$^{-1}$ deduced from the decay of the $6\,^3P_1$ fluorescence.

| | $k(^3P_1$-$^1D_2)$ | | $k_q(^1D_2)$ | |
|---|---|---|---|---|
| Noble gas | $T$ =775 K | $T$ =880 K | $T$ =775 K | $T$ =880 K |
| He | 71.6 ± 1.5 | | | |
| Ne | 35.2 ± 1.1 | 38.2 ± 1.1 | 3.1 ± 0.2 | 3.7 ± 0.2 |
| Ar | 38.8 ± 1.2 | 42.0 ± 1.2 | 0.28 ± 0.03 | 0.36 ± 0.03 |
| Kr | 20.5 ± 0.9 | 22.6 ± 0.9 | 0.077 ± 0.003 | 0.11 ± 0.02 |
| Xe | 5.2 ± 0.3 | 5.7 ± 0.3 | 3.0 ± 0.2 | 3.5 ± 0.2 |

TABLE V. Measured rate coefficients for collisional transfer processes studied in our experiment, in $10^{-12}$ cm$^3$ s$^{-1}$ at $T$ =880 K.

| Noble gas | $^3P_1$-$^1D_2$ | $^1D_2$-$^3D_3$ | $^3D_3$-$^3D_2$ | $^3D_2$-$^3D_1$ |
|---|---|---|---|---|
| He | 77 ± 16 | 115 ± 16 | 45 ± 9 | 60 ± 10 |
| | | 2.4[a], 2.8[b] | 9.8[a] | 6.6[a] |
| Ne | 40 ± 3 | 3.51 ± 0.18 | 0.32 ± 0.06 | 0.41 ± 0.04 |
| Ar | 43 ± 2 | 0.29 ± 0.04 | 0.11 +0.10 −0.04 | 0.20 ± 0.05 |
| | | 4.3[a] | 3.5[a] | 2.3[a] |
| | | | 0.192 ± 0.016[c] | 0.139 ± 0.013[c] |
| Kr | 22.9 ± 1.4 | 0.10 ± 0.04 | 0.02 +0.05 −0.015 | 0.045 ± 0.025 |
| Xe | 5.9 ± 0.3 | 3.28 ± 0.20 | 0.035 ± 0.020 | 0.39 ± 0.06 |

[a]Reference [22], $T$=1100 K.
[b]Reference [23], $T \approx$ 1000 K.
[c]Reference [35], $T$=857 K.

vide direct evidence of the $^1D_2$ population and the final state of the $^1D_2$ quenching process. The first column of Table V presents the rate coefficients for $^3P_1$-$^1D_2$ transfer found by the fitting of the absorption data to the complete rate equation model described above. Good agreement exists between these values and the corresponding rate coefficients derived from the fluorescence measurements (Table IV). This good agreement further confirms that the $^3P_1$-$^1D_2$ transfer process represents the major collisional depletion mechanism of the $^3P_1$ state, since

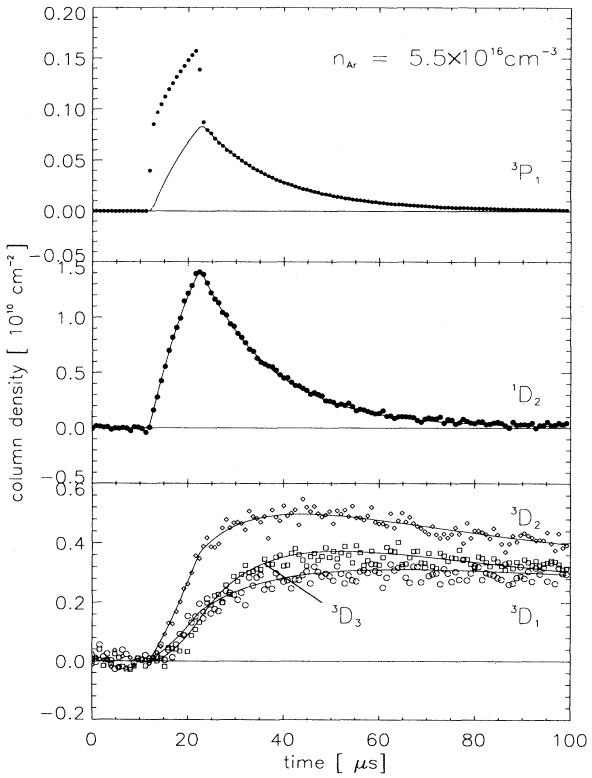


FIG. 8. Measured and fitted $^3P_1$ (top),$^1D_2$ (center), and $^3D_J$ (bottom) population densities vs time at an Ar density of 5.5 × 10$^{16}$ cm$^{-3}$ ($T$ =880 K, $\tau_p$ = 10 μs).

significant transfer to other states (e.g., 6 $^3P_0$) would add in first order to the fluorescence decay rate $\lambda_+$, raising the values in Table IV above those in Table V. This will allow us to impose upper limits on $^3P_J$ fine-structure mixing rates and on the rates for direct collisional transfer into the $^3D_J$ states.

### C. 5 $^1D_2$–5 $^3D_3$ transfer

While the collisional rate coefficient $k(^3P_1$-$^1D_2)$ only moderately depends on the noble-gas species, a quite different picture emerges for the transfer from the $^1D_2$ into the $^3D_3$ state, which shows a very strong dependence on the noble-gas (Table V). Figure 8 shows the measured transient population densities of $^3P_1$, $^1D_2$, and $^3D_J$ and the corresponding fits for an Ar density of 5.5 × 10$^{16}$ cm$^{-3}$. The $^1D_2$ population decays more slowly than at a Ne density of 2.2 × 10$^{16}$ cm$^{-3}$ (Fig. 4) and the $\chi^2$ fit reveals that in Ar a major part of the $^1D_2$ decay is due to collisional transfer back into the $^3P_1$ and subsequent radiative decay into the $^3D_{1,2}$ states. The importance of the back transfer is indicated by the solid line in the topmost panel of Fig. 8, which represents the part of the $^3P_1$ population that is due to back transfer from the $^1D_2$ state. It accounts for about 50% of the total $^3P_1$ population at the end of the laser pulse. The lower panel of Fig. 8 shows the $^3D_J$ population densities vs time. The $^3D_2$ population density, which is produced radiatively from the $^3P_1$ state, exhibits a delayed maximum due to the long tail of the $^3P_1$ population density. In contrast to the measurement at a Ne density of 2.2 × 10$^{16}$ cm$^{-3}$, the population in the $^3D_3$ state is now smaller than the population density in the $^3D_2$ state. The $\chi^2$ fit reveals that a major part of the $^3D_3$ population is produced by collisional transfer from the $^3D_2$ state. Figure 9, which shows the measured transfer rates for the process $^1D_2$-$^3D_3$ vs pressure, provides striking evidence for the strong dependence on the noble-gas.

The $^1D_2$-$^3D_3$ transfer rates obtained from the fits to the measurements at low Ar densities were systematically too low, and this is even more pronounced at low Kr

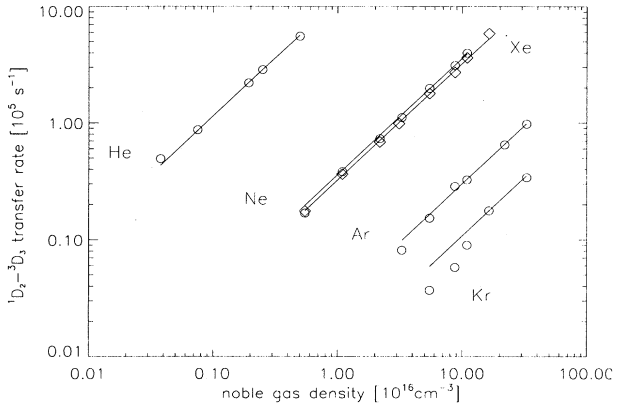


FIG. 9. Double-logarithmic plot of the $^1D_2$-$^3D_3$ transfer rate, demonstrating the strong dependence on the noble-gas species.

densities (Fig. 9). Since Ar and Kr are the weakest $^1D_2$ quenchers and therefore allow for long residence times in this state, we attribute this behavior to a possible breakdown of the assumption of equal diffusion coefficients for $^1D$ and $^3D$ states. Good agreement, within mutual error bars, exists between the $^1D_2$-$^3D_3$ transfer rates derived from the absorption measurement and the $^1D_2$ quenching rates found in the fluorescence measurements in Table IV at the same temperature.

### D. $5\,^3D_3$–$5\,^3D_2$, and $5\,^3D_2$–$5\,^3D_1$ transfer

Figure 10 shows the fractional population densities of the $^3D_J$ states vs time for a Ne density of $5.5\times10^{16}$ cm$^{-3}$. The solid lines represent the equilibrium values for the fine-structure components. The strong overpopulation of the $^3D_3$ state with respect to its equilibrium value corroborates its population out of the $^1D_2$ state. Furthermore,

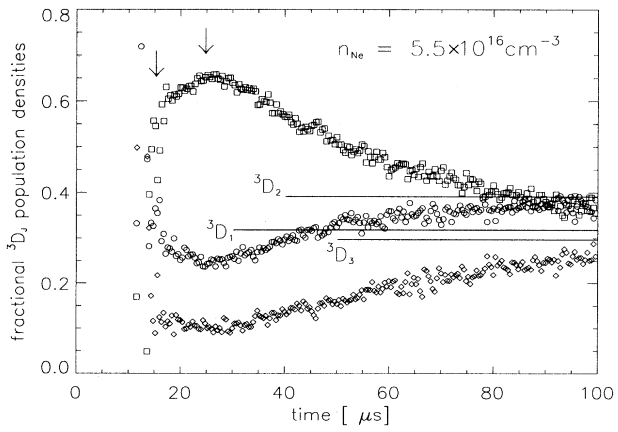


FIG. 10. Fractional population densities of the Ba $^3D_3$ (□), $^3D_2$ (◇), and $^3D_1$ (○) states vs time at a Ne density of $5.5\times10^{16}$ cm$^{-3}$. The solid lines represent the fractional equilibrium populations for $T$ =880 K. Arrows indicate the beginning of the laser pulse.

it can be seen that the $^3D_2$ population rises faster toward its equilibrium value than the $^3D_1$ population, although it decays into the latter. This indicates how the $\chi^2$ fit discerns that the $^3D_3$ population predominantly decays into the $^3D_2$ rather than the $^3D_1$ state.

Correlated with the deviations of the $^1D_2$-$^3D_3$ transfer rate at low Ar and Kr densities we find a large scatter of the $^3D_J$ intramultiplet rates, leading to the large errors given for the corresponding cross sections in Table V. We believe that this is also caused by our simplification in the treatment of diffusion.

### E. $6\,^3P_J$–$6\,^3P_{J'}$ and $6\,^3P_0$–$5\,^1D_2$ transfer

As mentioned above, no evidence has been found for a significant contribution of transfer channels other than the ones discussed so far. Including only these channels into our fits yielded good agreement with the experimental data. Nevertheless, we can estimate upper limits for some of the neglected collisional processes. For the fine-structure transfer within the $^3P_J$ states upper limits are imposed by the S/N ratio of our absorption measurements, which did not show any evidence of population of the $^3P_{2,0}$ states, by the good agreement between the rate coefficients for the $^3P_1$-$^1D_2$ transfer derived from the fluorescence and the absorption measurements, and by the time dependence of the $^3D_J$ populations, of which $^3D_{3,1}$ are radiatively connected to the $^3P_{2,0}$ states.

Within the detection limit of our absorption measurements of about 0.5% for the $^3P_{0,2}$ states, we found no evidence for population. This, however, does not impose a strong limit since we also never measured more than 3% absorption of the Ba line that probed the laser-pumped $^3P_1$ state. Since it is pumped directly, the latter can be expected to be more strongly populated than the $^3P_{0,2}$ states.

The good agreement between the rates coefficients for $^3P_1$-$^1D_2$ transfer derived from the fluorescence and the absorption measurements, respectively, also imposes an upper limit on possible $^3P_J$ fine-structure mixing rates. Due to the statistical errors of our measurements, ±10% uncertainty in the radiative rates of the transitions between $^3P_1$ and $^3D_{2,1}$ and about ±5% uncertainty of our determination of the relative oscillator strengths of the probe transitions, we estimate that the measured $^1D_2$ population rate coefficients are correct within ±15%. This allows the total rate coefficient for $^3P_1$ quenching to be at most 15% larger than the rate coefficient of the process $^3P_1$-$^1D_2$.

The third test for transfer into $^3P_{2,0}$ is provided by the time dependence of the $^3D_J$ populations. Since each $^3P_J$ state radiates into a very different mixture of $^3D_J$ states, $^3P_J$ mixing severely affects the ratios of $^3D_J$ populations. If $k(^3P_1$-$^3P_2)$ was included in the fit, the resulting transfer rate coefficients were less than 5% of $k(^3P_1$-$^1D_2)$. In our investigation of the possibility of $^3P_1$-$^3P_0$ transfer, we simultaneously allowed for $^3P_0$-$^1D_2$ collisional transfer since these processes are closely coupled; no evidence was found for either and we estimate $k(^3P_1$-$^3P_0)/k(^3P_1$-$^1D_2) \leq 0.05$. Our fitting procedure was very insensitive

to changes of the rate coefficient for the process $^3P_0$-$^1D_2$ leading to high upper limits: He, $2.6\times10^{-10}$ cm$^3$ s$^{-1}$; Ne, $1\times10^{-11}$ cm$^3$ s$^{-1}$; Ar, $6\times10^{-13}$ cm$^3$ s$^{-1}$; Kr, $6\times10^{-13}$ cm$^3$ s$^{-1}$; and Xe, $4\times10^{-11}$ cm$^3$ s$^{-1}$ at $T = 880$ K.

### F. $6\,^3P_1$–$5\,^3D_3$ transfer

Aside from the upper limit on $k(^3P_1$-$^3D_J)$, which is determined by the good agreement between the $^3P_1$-$^1D_2$ transfer rates determined in the fluorescence and absorption measurements, the quadratic rise of $^3D_3$ population with time allows us to improve these limits. Including the rate coefficient $k(^3P_1$-$^3D_3)$ into the fit we find upper limits of $k(^3P_1$-$^3D_3)/k(^3P_1$-$^1D_2) \leq 0.04$ for all noble-gases.

### G. $5\,^1D_2$–$5\,^3D_{1,2}$ and $5\,^3D_3$–$5\,^3D_1$ transfer

For experimental data taken under conditions where the $^3D_3$ peak population density is higher than that expected from the equilibrium distribution, the fit is very sensitive to inclusion of nonvanishing rate coefficients for the processes $^1D_2$-$^3D_{1,2}$. The reason is that due to detailed balancing the $^3D_{1,2}$ state cannot get rid of additional population by transfer into the $^3D_3$ state. In examining these data sets no evidence for these processes has been found for Ne, Ar, Kr, and Xe. Taking the accuracy of our determination of the relative population densities within the $^3D_J$ states as a measure of the accuracy of these collisional branching transitions, we conclude that $k(^1D_2$-$^3D_2)/k(^1D_2$-$^3D_3) \leq 0.05$, $k(^1D_2$-$^3D_1)/k(^1D_2$-$^3D_3) \leq 0.05$, and $k(^3D_3$-$^3D_1)/k(^3D_3$-$^3D_2) \leq 0.05$.

For He there was some indication of significant $5\,^1D_2$–$5\,^3D_2$, as well as $5\,^3D_3$–$5\,^3D_1$, transfer. In both cases this finding was not consistent for all measurements with He and we give conservative estimates of $k(^1D_2$-$^3D_2)/k(^1D_2$-$^3D_3) \leq 0.2$ and $k(^3D_3$-$^3D_1)/k(^3D_3$-$^3D_2) \leq 0.2$, which correspond to the maximum rate coefficients found by the $\chi^2$ fit. As with the heavier noble gases no evidence has been found for the transfer process $^1D_2$-$^3D_1$; therefore $k(^1D_2$-$^3D_1)/k(^1D_2$-$^3D_3) \leq 0.05$.

### H. Quenching of the $5\,^3D_J$ states

In order to find upper limits for the rate coefficients for the quenching process $^3D_J$-$^1S_0$ induced by collisions with noble-gas atoms, we included these rate coefficients, chosen to be equal for the three states in question, into the kinetic model for the population densities. The upper limits were estimated by comparing the results of the model with the data taken at high noble-gas pressures, where the data are most sensitive to this quenching. This allowed us to minimize the population decay due to diffusion. The upper limits of the rate coefficient were determined by finding the value of the rate coefficient that was no longer consistent with the data within its S/N ratio. This lead us to upper limits: He, $9\times10^{-14}$ cm$^3$ s$^{-1}$; Ne, $9\times10^{-15}$ cm$^3$ s$^{-1}$; Ar, $2\times10^{-15}$ cm$^3$ s$^{-1}$; Kr, $2\times10^{-15}$ cm$^3$ s$^{-1}$; and Xe, $3\times10^{-15}$ cm$^3$ s$^{-1}$ at $T = 880$ K. Since no special effort was undertaken to determine this limits by measuring at higher pressures or extending the time scale of the measurement to examine the long-time behavior of the $^3D_J$ populations, we do not expect this upper limits to be very stringent. However, these upper limits on the quenching rate coefficients are smaller by more than a factor of 10 than the rate coefficients for the dominant transfer processes, justifying the neglect of the quenching process in the kinetic model for the population densities.

## IV. DISCUSSION

As in previous measurements of multiplet mixing in alkaline earth metals induced by noble-gas collisions, we find a strong propensity for singlet-triplet mixing. The dominant decay channel is the transfer from $^3P_1$ to $^1D_2$ and subsequent $^1D_2$ transfer to $^3D_3$. No transfer between $^3P_1$ and $^3D_J$ has been observed and the fine-structure mixing within $^3P_J$ and $^3D_J$ is slower than the measured singlet-triplet transfer. Although a detailed explanation of the observed selectivity of the collisional transfer requires a theoretical calculation of the Ba–noble-gas potential curves, a qualitative discussion of the Ba–noble-gas interaction might provide some insight into the mechanisms causing the observed behavior.

Inspection of the qualitative potential curves for a Ba-NG system (Fig. 11), which only take into account the electrostatic part of the interaction, shows that the different multiplets are connected by the strongly repulsive $\Sigma$ potential curves. The potential curves and the corresponding molecular wave functions are denoted by $^{\Sigma}\Lambda_{\Omega}$, where $\Lambda$, $\Sigma$, and $\Omega$ are the projections of orbital, spin, and total angular momentum on the interatomic axis. In addition, electronic wave functions with $\Omega = 0$ are characterized by their behavior under reflection through a plane that contains the interatomic axis.

Taking spin-orbit coupling into account will lead to

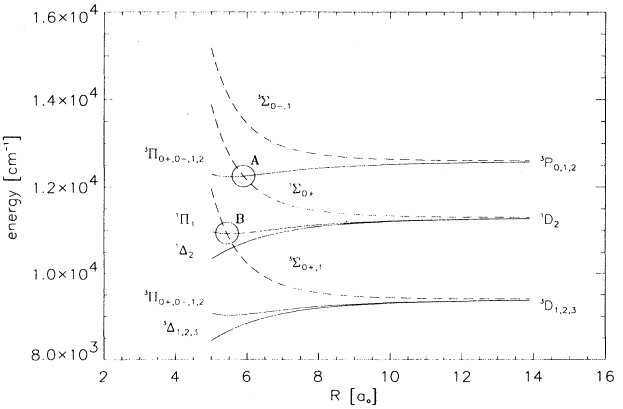


FIG. 11. Qualitative potential curves for a Ba-NG system, neglecting spin-orbit interaction. The relevant curve crossings are marked by circles $(A, B)$.

avoided crossings at the crossings of singlet and triplet potential curves ($A$ and $B$ in Fig. 11), and radial nonadiabatic coupling will cause nonadiabatic transitions at these avoided crossings. Selection rules for radial nonadiabatic coupling will allow $\Delta\Omega = 0$ transitions only [2]. Nonadiabatic transitions between potential curves with symmetry characters $0^+$ and $0^-$ are prohibited [33].

In this picture the transfer between $^3P_1$ and $^1D_2$ is due to radial coupling at the crossing of the $^3\Pi_{0^+}(^3P_1)$ curve originating from the $^3P_1$ state and $^1\Sigma_{0^+}(^1D_2)$, which is asymptotically correlated with the $^1D_2$ state (crossing $A$ in Fig. 11). The observed weak dependence of $k(^3P_1$-$^1D_2)$ on the noble-gas species and on temperature (Table IV) indicates strong nonadiabatic coupling or, equivalently, only a weakly avoided curve crossing. For the $^3\Pi_{0^+}(^3P_1)$ and $^1\Sigma_{0^+}(^1D_2)$ crossing, the strength of spin-orbit coupling is determined by the admixture of $^1\Sigma_{0^+}(^1P_1)$ to the $^1\Sigma_{0^+}(^1D_2)$ orbital, which depends on the coupling of these states by the electrostatic interaction with the noble-gas atom. Due to the large energy splittings between those states the electrostatic mixing can still be limited and therefore cause no strong repulsion of the potential curves at the crossing point.

A striking result of our experiment with Ba is the very strong noble-gas dependence of $k(^1D_2$-$^3D_3)$. This is in contrast to the rate coefficients for the equivalent transfer process in Sr [19], which shows only a weak perturber dependence. The transfer between the $^1D_2$ and the $^3D_3$ state is most likely caused by radial coupling at the crossing of the $^1\Pi_1(^1D_2)$ and $^3\Sigma_1(^3D_3)$ terms [14] (crossing $B$ in Fig. 11). The energy gap between these two adiabatic curves at the avoided crossing is proportional to the $^3D$ fine-structure constant [14], which is about 4 times larger for the Ba $6s5d\,^3D_J$ states than for the corresponding Sr $5s4d\,^3D_J$ states. The difference between the cross sections for this particular process in Sr– vs Ba–noble-gas collisions indicates a change in the characteristics at the avoided crossing from almost sudden to nearly adiabatic.

The exclusive production of the $^3D_3$ state in the $^1D_2$-$^3D_J$ transfer process and the small rate coefficients for $^3D_J$ fine-structure mixing provide evidence for another transition from the sudden regime for Ca and Sr into the nearly adiabatic regime for Ba. These processes are closely related. The branching fraction for the three different $^3D_J$ states is determined by the $J$ mixing in the outgoing half collision of a $^1D_2$-$^3D_J$ transfer process when the system evolves along the $^3\Sigma_1(^3D_J)$ potential curve, which is adiabatically correlated to the $^3D_3$ state. The $^3D_J$ fine-structure mixing is the result of a full collision of an atom originally in a $^3D_J$ state. For Ca–noble-gas collisions Breckenridge and Merrow report a production of all $^3D_J$ states close to their statistical weight in the transfer process $4\,^1P_1$-$3\,^3D_J$ [9]. The same result has been reported by Miller *et al.* for the collision process $^1D_2$-$^3D_J$ in Sr. In Ba-NG collisions where the $5\,^3D_J$ fine-structure splitting is about 4 times larger than in Sr $4\,^3D_J$ we found no indication for collisional transfer from $5\,^1D_2$ into $5\,^3D_{2,1}$ and only weak fine-structure mixing, except for He. The lack of $^3D_{1,2}$ production agrees very well with Breckenridge and Merrow's findings for transfer between $6\,^1P_1$ and $6\,^3P_J$ in Ba [21], which show transfer into $^3P_2$ only. Qualitatively our results for $^3D_J$ fine-structure mixing are in good agreement with Kelly's results for noble-gas-induced fine-structure transfer in the $5\,^3P_J$ state of Sr [20], which has almost the same fine-structure splitting as the Ba $5\,^3D_J$ states and exhibits nearly adiabatic behavior of the collision complex. As in our experiment the measured rate coefficients show a strong decrease from He to Ne collisions but a weak dependence on the heavier noble-gas species. The difference in magnitude of the rate coefficients between our results and those of Kelly, whose rate coefficients are two orders of magnitude smaller, might be due in part to the lower temperature ($T$=680–800 K) in Kelly's experiment or simply to different atomic interactions.

With Xe perturbers the rate coefficients for the processes $^1D_2$-$^3D_3$ and $^3D_2$-$^3D_1$ show deviations from the general behavior described above, while the transfer probability for the process $^3D_3$-$^3D_2$ follows the general trend. Such irregular behavior in collisional processes involving Ca and Xe has been reported before [8] and was attributed to favorable curve crossings in the Ca-Xe quasimolecule.

Also shown in Table V are the rate coefficients for the processes $^1D_2$-$^3D_J$, $^3D_3$-$^3D_2$, and $^3D_2$-$^3D_1$ measured by Kallenbach and Kock [22] for He and Ar ($T$ =1100) and the value for the former process with He perturbers at $T \approx 1000$ K reported by Bowen and Thorne [23]. In both experiments the $6\,^1P_1$ resonance state of Ba was strongly pumped with a pulsed dye laser and the time evolution of the lower-lying states was monitored by a time-resolved Hook technique. The Ba density in these experiments was $2\times10^{14}$ cm$^{-3}$. Kallenbach and Kock derived their rate coefficients by fitting their experimental data to a complex 13-level rate equation model including inelastic Ba-noble-gas, Ba-Ba, and Ba-$e^-$ collisions, photoionization, Penning ionization, and associative ionization [34]. Bowen and Thorne, who also had to account for Ba-Ba collisions, determined $k(^1D_2$-$^3D_J)$ by measuring the lifetime of the $^1D_2$ state vs Ba and noble-gas density. Kallenbach and Kock report values for Ba-Ar collisions about ten times larger and for He ten times smaller than the rate coefficients measured in our experiment. Their rate coefficient for the process $^1D_2$-$^3D_J$ induced by He agrees well with the value reported by Bowen and Thorne. Since, as discussed above, these transfer processes show nearly adiabatic behavior in the Ba-Ar case, the larger value at 1100 K might be explained by an exponential temperature dependence of the rate coefficient for a nearly adiabatic process. The disagreement in the He case, however, cannot be explained in this manner.

Reasonable agreement within mutual error bars exists between our results and and the rate coefficients for Ar-induced $^3D_J$ fine-structure mixing determined in a very recent experiment by Ehrlacher and Huennekens [35]. In an experiment dedicated to determine these mixings the $^3D_2$ state was populated by stimulated emission from the laser-pumped $^3P_1$ state. The population densities of the $^3D_J$ states were then monitored by time-resolved absorption spectroscopy. The results of this measurement are also shown in Table V.

Kallenbach and Kock report rate coefficients for $^3P_J$

fine-structure mixing induced by collisions with He and Ar perturbers that are more than two orders of magnitude smaller than our $k(^3P_1\text{-}^1D_2)$, which indicates why we found no evidence for $^3P_J$ fine-structure transfer in our experiment. In agreement with our findings none of the experiments mentioned above provided evidence for quenching of the $^3D_J$ states by collisions with noble-gas atoms.

## V. CONCLUSION

We have measured the cross sections for collisional transfer between the low-lying excited states of Ba induced by collisions with noble-gas atoms. We found that the collisional transfer between the excited $6\,^3P_1$ and the metastable $5\,^3D_J$ states is dominated by singlet-triplet transfer. The main transfer channels are $6\,^3P_1\text{-}5\,^1D_2$ and $5\,^1D_2\text{-}5\,^3D_3$. The cross section of the former shows only a weak dependence on the noble gas while the cross section for the latter changes over almost three orders of magnitude, generally decreasing with increasing noble-gas mass. The fine-structure mixing rate coefficients for the $5\,^3D_J$ states and their dependence on the noble-gas species qualitatively agree with previous measurements of fine-structure mixing of the $5\,^3P_J$ states of Sr. We find no indication for significant fine-structure mixing within the $6\,^3P_J$ states or of direct collisional transfer from $6\,^3P_J$ to $5\,^3D_J$. We hope theoretical studies will further investigate these collision processes and improve our understanding of collisions between two-electron atoms and noble gases.

## ACKNOWLEDGMENTS

This work was supported by the National Science Foundation, Grant No. PHY90-12244 to the University of Colorado. We are grateful to J.A. Neuman for building parts of the experimental apparatus and helpful discussion. J.B. thanks the Hochschulsonderprogram II of the German Academic Exchange Service (DAAD) for providing financial support.

[1] L. Krause, in *The Excited State in Chemical Physics*, edited by J. W. McGowan (Wiley, New York, 1975), p. 267.
[2] E. E. Nikitin, in *The Excited State in Chemical Physics*, edited by J. W. McGowan (Wiley, New York, 1975), p. 267.
[3] R. W. Anderson, J. Chem. Phys. **77**, 5426 (1986).
[4] T. S. Monteiro, I. L. Cooper, A. S. Dickinson, and E. L. Lewis, J. Phys. B **19**, 4087 (1986).
[5] J. Brust, M. Movre, and K. Niemax, Z. Phys. D **27**, 243 (1993).
[6] B. Pouilly, T. Orlikowski, and M. Alexander, J. Phys. B **18**, 1953 (1985).
[7] J. J. Wright and L. C. Balling, J. Chem. Phys. **73**, 1617 (1980).
[8] M. Harris, D. R. McHugh, E. L. Lewis, I. Shannon, and M. Zokai, J. Phys. B **20**, 5575 (1987).
[9] W. H. Breckenridge and C. N. Merrow, J. Chem. Phys **88**, 2320 (1988).
[10] M. O. Hale and S. R. Leone, J. Chem. Phys. **79**, 3352 (1983).
[11] M. O. Hale, I. V. Hertel, and S. R. Leone, Phys. Rev. Lett. **53**, 2296 (1984).
[12] A. Z. Devdariani and A. L. Zagrebin, Chem. Phys. Lett. **131**, 197 (1986).
[13] E. Czuchaj, F. Rebentrost, H. Stoll, and H. Preuss, Chem. Phys. **138**, 303 (1989).
[14] A. L. Zagrebin and S. I. Tserkovnyi, Opt. Spectrosc. **75**, 161 (1993).
[15] H.-J. Yuh and P. J. Dagdigian, Phys. Rev. A **28**, 63 (1983).
[16] M. H. Alexander, T. Orlikowski, and J. E. Straub, Phys. Rev. A **28**, 73 (1983).
[17] A. R. Malvern, J. Phys. B **11**, 831 (1978).
[18] E. N. Borisov, N. P. Penkin, and T. P. Redko, Opt. Spectrosc. **63**, 277 (1988).
[19] D. A. Miller, L. You, J. Cooper, and A. Gallagher, Phys. Rev. A **46**, 1303 (1992).
[20] J. F. Kelly, M. Harris, and A. Gallagher, Phys. Rev. A **37**, 2354 (1988).
[21] W. H. Breckenridge and C. N. Merrow, J. Chem. Phys. **88**, 2329 (1988).
[22] A. Kallenbach and M. Kock, J. Phys. B **22**, 1705 (1989).
[23] J. L. Bowen and A. P. Thorne, J. Phys. B **18**, 35 (1985).
[24] J. A. Neuman, A. C. Gallagher, and J. Cooper, Phys. Rev. A **50**, 1292 (1994).
[25] T. G. Walker, K. D. Bonin, and W. Happer, J. Chem. Phys. **87**, 660 (1987).
[26] C. H. Corliss and W. R. Bozman, *Title*, Natl. Bur. Stand. (U.S.) Monograph 53 (U.S. GPO, Washington, DC, 1962), p. 9.
[27] L. Jahrreis and M. C. E. Huber, Phys. Rev. A **31**, 692 (1985).
[28] S. Niggli and M. C. E. Huber, Phys. Rev. A **35**, 2908 (1987).
[29] S. Niggli and M. C. E. Huber, Phys. Rev. A **39**, 3924 (1989).
[30] W. H. Parkinson and F. S. Tomkins, J. Opt. Soc. Am. **68**, 535 (1978).
[31] C. W. Bauschlicher, R. L. Jaffe, S. R. Langhoff, F. G. Mascarello, and H. Partridge, J. Phys. B **18**, 2147 (1985).
[32] H. Bucka and H. H. Nagel, Ann. Phys. (Leipzig) **8**, 329 (1961).
[33] E. I. Dashevskaya, A. I. Voronin, and E. E. Nikitin, Can. J. Phys. **47**, 1237 (1969).
[34] A. Kallenbach and M. Kock, J. Phys. B **22**, 1691 (1989).
[35] E. Ehrlacher and J. Huennekens, Phys. Rev. A **50**, 4786 (1994).